

<sup>1</sup> **Can Large-Scale Clustering of Tropical Precipitation  
Be Used to Constrain Climate Sensitivity?**

<sup>3</sup> **P. Blackberg<sup>1,2</sup>, M. S. Singh<sup>1,2</sup>**

<sup>4</sup> <sup>1</sup>School of Earth, Atmosphere, and Environment, Monash University, Victoria, Australia

<sup>5</sup> <sup>2</sup>Centre of Excellence for the Weather of the 21st Century, Monash University, Victoria, Australia

6      **Abstract**

7      The spatial organization of deep convection in tropical regions is posited to play an im-  
 8      portant role in determining characteristics of the tropical climate such as the humidity  
 9      distribution and cloudiness and may therefore be an important control on climate feed-  
 10     backs. This study analyzes one aspect of convective organization, the clustering of heavy  
 11     precipitation on large scales, in both interannual variability and under warming in fu-  
 12     ture climate projections. Clustering is quantified using the top 5% heaviest daily pre-  
 13     cipitation instances, and interpreted as increasing with the area covered by heavy pre-  
 14     cipitation ( $C$ , temporally clustered rainfall) and proximity of heavily rainy points to each  
 15     other and to key zonal and meridional reference lines ( $P$ , orthogonal to coverage). Both  
 16     observations and global climate models (GCMs) indicate temporal clustering of heavy  
 17     rainfall is best described by the tropical-mean precipitation rate ( $r \sim 0.55 - 0.85$ ) and  
 18     spatial clustering is favored by El Niño conditions, but observed and modelled deseason-  
 19     alized interannual variability importantly diverge in the tropical-mean relative humid-  
 20     ity and low cloudiness associated with spatially clustered states. Under future warming,  
 21     all models from the CMIP6 ensemble project an increase in clustering associated with  
 22     a narrowing of the intertropical convergence zone and with a model-spread partially ex-  
 23     plained by differences in projections of the Pacific SST gradient ( $r=-0.46$ ). However, un-  
 24     like variability, changes in general spatial clustering with warming do not explain the cli-  
 25     matological humidity or low-cloud responses, limiting a simple observational constraint  
 26     on feedbacks. Notably a few model outliers drive considerable spread in tropical-mean  
 27     mid-tropospheric drying ( $r=0.44$ ) linked to a climatological meridional clustering of heavy  
 28     rainfall, suggesting potential for future model evaluation.

29      **Plain Language Summary**

30      The spatial distribution of rainfall in the tropics is expected to change in a warm-  
 31     ing climate, with potentially important impacts on how much radiation is absorbed by  
 32     water vapor and reflected by clouds. This study shows that heavy rainfall tends to move  
 33     towards the equator and to the Pacific Ocean in projections with global climate mod-  
 34     els, resulting in an overall increase in the "clustering" of rainfall on the large scale. Fur-  
 35     ther, the results show a shift in rainfall to the equator with global warming is associated  
 36     with a drying of the tropical atmosphere, which may have an influence on how much the  
 37     planet warms for a given  $CO_2$  change. However, similar observed shifts in rainfall in the  
 38     current climate are not found to have the same effect on humidity and clouds as for changes  
 39     with warming, suggesting caution should be exercised when using relationships derived  
 40     from observations to predict future changes.

## 41 1 Introduction

42 The spatial organization of deep convection in tropical regions plays a critical role  
 43 in shaping the hydrological cycle and the moisture and cloud distribution (Hartmann  
 44 et al., 1984). Changes in organization with warming may therefore have implications for  
 45 a range of climatic processes, including precipitation extremes (e.g., Pendergrass et al.,  
 46 2016; Bao et al., 2017; Semie & Bony, 2020) and the radiative feedbacks that control equi-  
 47 librium climate sensitivity (ECS) (e.g., Emanuel et al., 2014; Bony et al., 2020; Schiro  
 48 et al., 2022). However, because many of the relevant small-scale processes are not resolved  
 49 in climate models, it remains unclear how convective organization will evolve in a warmer  
 50 climate.

51 While there are numerous ways by which convection may organize, one important  
 52 mechanism is the clumping or clustering together of convective elements (e.g., Maddox,  
 53 1980; Mapes, 1993; Bretherton et al., 2005). Such clustering occurs on a range of scales  
 54 (Mapes & Houze, 1993), including at large scales that are resolved by climate models  
 55 and at mesoscales that can typically only be resolved in high-resolution storm-resolving  
 56 simulations. Recently, Bläckberg & Singh (2022) showed that the extent to which trop-  
 57 ical precipitation exhibits clustering on the large scale increases with warming in climate  
 58 projections from the Coupled Model Intercomparison Project phase 5 (CMIP5). This  
 59 large-scale clustering is distinct from other types of organization on the mesoscale, but  
 60 idealized simulations suggest that similar processes may act at both scales, and that both  
 61 large-scale and mesoscale organization of convection may modulate the radiation bud-  
 62 get (Wing et al., 2018).

63 Here we build on the work of Bläckberg & Singh (2022), showing that increased  
 64 clustering of heavy precipitation with warming is a robust feature of the more recent CMIP6  
 65 as well as CMIP5. Further, we explore the mechanisms that lead to large-scale cluster-  
 66 ing of precipitation in the tropics and the influence of an increase in clustering on prop-  
 67 erties of the atmosphere that are important for the radiation budget. The analysis will  
 68 compare how clustering varies across different timescales, from interannual variability  
 69 in both models and observations to changes in the climatological clustering of convec-  
 70 tion in a warming climate. This approach allows us to assess whether observational con-  
 71 straints of convective organization under current climate conditions can help constrain  
 72 changes in organization and the associated radiative feedbacks with warming.

73 Previous studies have highlighted observed relationships between convective organi-  
 74 zation and the tropical radiation budget (Tobin et al., 2013; Holloway et al., 2017; Bony  
 75 et al., 2020). For example, Bony et al. (2020) find tropical mesoscale convective organi-  
 76 zation and Estimated Inversion Strength (EIS) in subsidence regions are the two strongest  
 77 predictors of deseasonalized interannual variability in net top-of-atmosphere radiation,  
 78 together explaining about 60 percent of the variance. While the two predictors are sig-  
 79 nificantly correlated and potentially partly mechanistically connected (Williams et al.,  
 80 2023), the authors find that both have an independent contribution in influencing the  
 81 tropical radiation budget; EIS is found to have a stronger correlation with the cloudy  
 82 component of the radiation budget while convective organization is found to have a stronger  
 83 connection to the clear-sky component of the radiation budget. Bony et al. (2020) ar-  
 84 gue that clustering of deep convective elements is associated with a tropical-mean dry-  
 85 ing, resulting in increased outgoing longwave radiation due to a reduction in the green-  
 86 house effect.

87 This hypothesis is supported by idealized studies of convective “self-aggregation”  
 88 (e.g., Wing & Emanuel, 2014). Both cloud-resolving and climate-model simulations run  
 89 in idealized settings reminiscent of tropical conditions (i.e., low rotation rate and weak  
 90 temperature gradients) show increased outgoing longwave radiation when convection is  
 91 more clustered within the domain (Wing et al., 2018).

The preceding studies suggest that increased clustering of convection with warming may lead to a negative clear-sky feedback from clustering-induced drying, resulting in reduced equilibrium climate sensitivity (ECS) (Emanuel et al., 2014). However, recent research suggests that clustering of deep convection on the large scale may also be indirectly connected to a positive shortwave feedback on warming through changes in low clouds (Schiro et al., 2022). According to this argument, drying associated with increased clustering of convection is controlled by the large-scale overturning circulation and is most pronounced in regions of climatological descent where low-cloudiness is sensitive to changes in relative humidity. The associated cloud changes then lead to a net positive feedback.

As the above discussion highlights, an important control on convective organization at both large- and mesoscales comes from large-scale circulation patterns, including the Intertropical Convergence Zone (ITCZ), the South Pacific Convergence Zone (SPCZ), the Walker circulation, and convectively-coupled tropical waves (Bony et al., 2020; Quan et al., 2025; Arnold & Randall, 2015; Wodzicki & Rapp, 2016; Wheeler & Kiladis, 1999). Changes to the clustering of precipitation under warming may therefore be linked to, for example, a “narrowing” of the ITCZ due to constraints on the export of energy by the Hadley cell (Byrne & Schneider, 2016) or changes in the Walker circulation driven by changes in zonal SST gradients (Quan et al., 2025), which may be associated with “El Niño-like” shifts in the SST climatology (Watanabe et al., 2024).

The existing literature show large-scale clustering is projected to increase from the forced response of global warming, and that a more clustered state in observed interannual variability, albeit on a different spatial scale, is associated with clear-sky and cloud-radiative feedbacks. In this study we elucidate to what extent observed and modelled interannual variability in large-scale clustering of heavy precipitation connects to similar radiative feedbacks and whether such relationships can be used to constrain climate sensitivity. To do so, we quantify and relate clustering of heavy rainfall to the tropical-mean and distribution of relative humidity and low-cloudiness in observations, a high-resolution GCM from the NextGEMS pre-final cycle, and GCMs from the CMIP6 ensemble (method described in Section 2). The results of this study adds to the existing literature by describing the spatial patterns of heavy rainfall that promote large-scale clustering (Section 3), the associated mechanisms involving SST patterns and a narrowing of the ITCZ (Section 4), and the tropical radiative feedbacks associated with a more clustered state (Section 5) in interannual variability and for projected climatological changes with warming. Section 6 gives a summary of the key findings and an outlook for future research.

128 **2 Data and Methods**

129 Our analysis is focused on variations in the large-scale clustering of heavy precip-  
 130 itation in the tropics and its relationship to the atmospheric state in both observations  
 131 and an ensemble of global climate models (GCMs) primarily from CMIP6. We begin by  
 132 describing the datasets (both model and observational) used, before we describe the quan-  
 133 tification of large-scale clustering, and our analysis framework.

134 **2.1 Models**

135 We use simulations from 27 GCMs from CMIP6 (Eyring et al., 2016), using data  
 136 from the years 1970-1999 in the historical scenario, representing the current climate, and  
 137 from the years 2070-2099 under the Shared Socioeconomic Pathway 585 (SSP5-8.5), rep-  
 138 resenting a warmer climate. The models are chosen based on availability of the required  
 139 variables and are shown in Figure 6. We use one ensemble member from each model.

140 In addition to the CMIP6 models, we also consider a simulation using a high-resolution  
 141 GCM referred to here as IFS\_9\_FESOM\_5 (Koldunov et al., 2023). The Deutsches Kli-  
 142 marechenzentrum (DKRZ) Next Generation Earth Modelling Systems (NextGEMS) pre-  
 143 final cycle provides high-resolution globally simulated atmospheric and oceanic variables  
 144 for SSP3-7.0 forcing between 2025-2049 using the ECMWF Integrated Forecasting Sys-  
 145 tem (IFS) at  $\sim 9$  km horizontal grid spacing for the atmosphere and the Finite-VolumE  
 146 Sea Ice-Ocean model version 2 (FESOM2) at 5 km horizontal grid spacing for the ocean  
 147 (Koldunov et al., 2023). Although the model is at high resolution compared to the CMIP6  
 148 models, it retains a convection parameterization, and we therefore describe it as a GCM  
 149 rather than a storm-resolving model. Because the climate change signal during the sim-  
 150 ulation is small, we only use the high-resolution GCM to characterize interannual vari-  
 151 ability, using all available years.

152 **2.2 Observations**

153 Observed clustering of tropical precipitation is quantified based on daily precip-  
 154 itation estimates from the National Oceanic and Atmospheric Administration Global Pre-  
 155 cipitation Climatology Project (NOAA-GPCP) (Huffman et al., 2023), using the method  
 156 described in the next subsection. We further use NOAA-GlobalTemp (Huang et al., 2024),  
 157 and Clouds and the Earth's Radiant Energy System (CERES) data (Doelling et al., 2013)  
 158 to provide observational estimates of surface temperature and Top of the atmosphere ra-  
 159 diative fluxes, respectively. Estimates of vertical pressure velocity and specific and rel-  
 160 ative humidity are taken from the fifth generation of the European Centre for Medium-  
 161 Range Weather Forecasts reanalysis (ERA5) (Hersbach et al., 2023). Apart from pre-  
 162 cipitation, all variables are taken as monthly averages.

163 Finally, we develop a simple estimate of the low-cloud fraction using the tropical  
 164 weather states defined in Tselioudis et al. (2010) based on data from the International  
 165 Satellite Cloud Climatology Project (ISCCP) (Young et al., 2018). Tselioudis et al. (2010)  
 166 used a clustering algorithm to categorize histograms of cloud-top pressure and optical  
 167 thickness given by the ISCCP D1 dataset into a series of weather states defined in three  
 168 hourly polar-orbiting satellite scans with daily global coverage on a  $1^\circ \times 1^\circ$  grid. Each  
 169 weather state is characterized by a histogram in cloud-top pressure and optical thick-  
 170 ness that represents the centroid over all members of that weather state. Here we esti-  
 171 mate the cloud fraction as a function of pressure for a given weather state as the total  
 172 frequency of clouds of all optical thicknesses in a given range of cloud-top pressure within  
 173 the corresponding centroid histogram. We then calculate the low-cloud fraction  $LCF_i$   
 174 of weather state  $i$  as the total cloud fraction below 600 hPa. The monthly low-cloud frac-  
 175 tion is taken as

$$LCF = \sum_i f_i LCF_i, \quad (1)$$

176 where  $f_i$  is the frequency of weather state  $i$  over the month in question.

177 As described further below, all observational datasets are regridded conservatively  
 178 to a common  $2.8^\circ \times 2.8^\circ$  grid for analysis. We use observations covering the time pe-  
 179 riod between 1998-2023 for all datasets, except for cloud fraction (based on ISCCP), which  
 180 is limited to 1998-2017.

### 181 2.3 Quantifying Large-Scale Clustering of Heavy Precipitation

182 We quantify clustering of precipitation following Bläckberg & Singh (2022) using  
 183 daily surface precipitation in the tropics ( $30^\circ\text{S}$ - $30^\circ\text{N}$ ). To facilitate the comparison of clus-  
 184 tering across different models and the observations, we first interpolate the daily precip-  
 185 itation to a  $2.8^\circ \times 2.8^\circ$  grid using a first-order conservative method (Jones, 1999) to pre-  
 186 serve tropical-mean properties from the native grid. Next we define heavily precipitat-  
 187 ing regions as gridboxes for which the precipitation rate exceeds a threshold. The thresh-  
 188 old is calculated as the 95th spatial percentile of daily precipitation over all gridboxes  
 189 in the tropics temporally averaged over the 30-year climatology (or 25-year in the case  
 190 of observations and the high-resolution model). For the GPCP observations, this thresh-  
 191 old is  $16 \text{ mm day}^{-1}$  and in models the interquartile range in thresholds is  $15\text{-}17 \text{ mm day}^{-1}$ .  
 192 Distinct heavy precipitation features are identified as 8-connected contiguous regions of  
 193 precipitation exceeding the threshold or single grid boxes if there are no neighboring con-  
 194 nections. While there are conceptual differences in what type of rainfall that is repre-  
 195 sented by different percentile thresholds, overall conclusions of the paper is not sensitive  
 196 to using the 90th, 95th, or 97th percentile.

197 We define our primary measure of clustering,  $A_m$ , as the mean area of heavy pre-  
 198 cipitation features over the entire tropics.  $A_m$  conceptually captures clustering by dis-  
 199 tinguishing scenes with many small precipitation features and scenes where precipita-  
 200 tion is aggregated into fewer and/or larger precipitating features (Figure 1 and Figure  
 201 3c). The mean area of features,  $A_m$ , was chosen due to its interpretability, however, we  
 202 note that it is only one aspect of the large-scale organization of precipitation, and alone  
 203  $A_m$  does not describe important spatial characteristics such as the total area coverage,  
 204 proximity, location, shape, and gradients of precipitation intensity of precipitation fea-  
 205 tures. A number of other measures of large-scale clustering are analyzed and the inter-  
 206 relationship between a subset of metrics is presented in Figures S1-2 in the supporting  
 207 information. An important aspect of our method is that, by definition, regions of heavy  
 208 precipitation occupy 5% of the domain on average. Thus when comparing two climates,  
 209 the time-mean area covered by heavy precipitation  $\bar{C}$  remains constant. Differences in  
 210 the mean area of features,  $A_m$ , between climates are entirely due to a reorganization of  
 211 precipitation, where an increase in  $A_m$  increases the general proximity of heavily pre-  
 212 precipitating points to each other in that the number of distinct precipitation features ( $N$ )  
 213 is reduced (proportional as reciprocals for the same total area coverage,  $A_m = C/N$ ).  
 214 However, the above constraint does not apply to the precipitation distribution during  
 215 a given month. Indeed, as we shall see, an important driver of variations in tropical pre-  
 216 cipitation clustering in interannual variability is the area coverage of heavy precipita-  
 217 tion,  $C$ . We therefore consider the behavior of both the mean area of heavy precipita-  
 218 tion features,  $A_m$ , and the area coverage of heavy precipitation,  $C$ , in our analysis be-  
 219 low.

### 220 2.4 Describing Relationships to Large-Scale Clustering of Heavy Pre- 221 cipitation

222 Having quantified large-scale precipitation clustering, we seek to characterize the  
 223 relationships between such clustering and other large-scale climate variables. Specifically,  
 224 we consider these relationships for interannual variability in both models and observa-  
 225 tions, and for changes in climate across the CMIP6 ensemble. Throughout, we define in-

terannual variability in a given variable by deseasonalized monthly anomalies, calculated as the monthly-mean anomaly from the climatology of the associated month after detrending the time series. The trend is estimated by a first-order linear least squares regression of the data at each location from the daily (precipitation-based metrics) or monthly (all other metrics) time series. However, relationships are consistent regardless of whether the linear trend is removed or not.

As we will see, for interannual variability, the mean area of features,  $A_m$ , and the area coverage of precipitation,  $C$ , are strongly correlated with each other and to the large-scale climatic state. The total area coverage of heavy precipitation,  $C$ , is primarily interpreted in the present framework as a confounding variable, partly connected to the tropical-mean temperature, but best described by the tropical-mean rainfall rate ( $r \sim 0.35$  and  $r \sim 0.86$  respectively in Figure S1 in supporting information). However, the variations in total coverage of heavy precipitation can also be viewed as a tropical temporal clustering of rainfall independent of spatial clustering (Figure 3c, x-axis). To estimate the individual effect of the general spatial clustering or proximity of heavily precipitating points to each other, analogous to the climatological change in  $A_m$  with warming (Figure 3c, y-axis), we apply the method of Pearson partial correlation (Mardia et al., 1979). The partial correlation  $r(X, Y|Z)$  represents the relationship between variables  $X$  and  $Y$  after the removal of the effect of  $Z$ , and is given by

$$r(X, Y|Z) = \frac{r(X, Y) - r(X, Z)r(Y, Z)}{\sqrt{1 - r^2(X, Z)}\sqrt{1 - r^2(Y, Z)}}, \quad (2)$$

where  $r(X, Y)$  is the regular correlation between  $X$  and  $Y$ . For partial correlations and simple linear regression, relationships are considered significant if the correlation coefficient is large relative to its uncertainty, as quantified by a standard two-sided t-test, such that the probability of observing a correlation by chance under the null hypothesis of no correlation is below 5%. However, further robustness testing is applied for model-spread correlations, in which potential outliers are removed before calculating the correlation and significance.

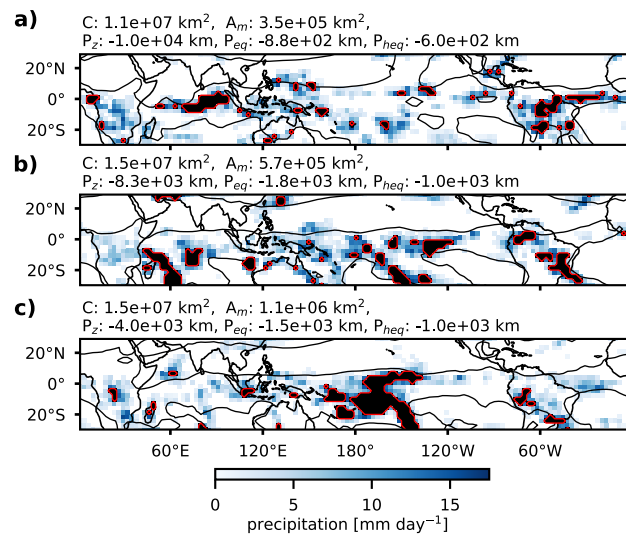


**Figure 1.** February daily snapshots of GPCP precipitation (blue colors) and heavy precipitation features (black shading), with monthly specific humidity representing the median over the tropics (black contour). The panel titles show the total area coverage of heavy precipitation,  $C$ , and the mean area of precipitation features,  $A_m$ , with the proximity of heavily precipitation points to the central pacific, equator, and hydrological equator below (described in greater detail in Figure 4).

### 252 3 Spatial Patterns of Heavy Rainfall Clustering

253 Both The purpose of this section is to elucidate the spatial patterns of precipitation  
 254 that produce a high degree of clustering. We first consider how clustering changes  
 255 in interannual variability before we investigate the spatial patterns associated with in-  
 256 creases in clustering with warming across the CMIP6 ensemble.

257 Figure 2 shows the regression of monthly anomalies in the frequency of occurrence  
 258 of heavy precipitation,  $FOO$ , onto the mean area of heavy precipitation features,  $A_m$ ,  
 259 for the observations. When tropical precipitation is observed to be highly clustered on  
 260 the large scale, heavy precipitation tends to occur more frequently in the central equa-  
 261 torial Pacific. Figure 2 is calculated for all months, but similar spatial patterns can be  
 262 seen in individual months, strongest in DJF (Figure S3 in the supporting information).  
 263 Other notable spatial characteristics of the regression include a decrease in heavy pre-  
 264 cipitation over the maritime continent and a small but statistically significant (crosses)  
 265 decrease in heavy precipitation over the Amazon and Atlantic.

266 To quantify the shift of heavy precipitation to the central equatorial Pacific, we de-  
 267 fine the proximity metrics  $P_z$ , which represents the mean distance of heavily precipitat-  
 268 ing points within the tropics to the meridian given by the longitude  $180^\circ\text{E}$ , and  $P_{eq}$  and  
 269  $P_{heq}$ , which represents a similar metrics defined based on distance to the geographic- and  
 270 hydrological equator (Figure 4 schematic). Here the hydrological equator is defined as the  
 271 latitude of highest specific humidity at 700 hPa as a function of longitude and time in  
 272 months. These are somewhat arbitrary zonal and meridional reference lines with which  
 273 to describe the zonal and meridional shifts, and the clustering redistribution of heavy  
 274 precipitation may be better characterized relative to the climatological distribution. For  
 275 example, in most models, with warming heavy precipitation moves south relative to the  
 276 northern hemisphere climatological convergence zone or north relative the climatolog-  
 277 ical SPCZ or both. However, for simplicity, we use  $P_z$ ,  $P_{eq}$ , and  $P_{heq}$  defined based on  
 278  $180^\circ\text{E}$  and the equator.

279 As expected from the regression map, there is a strong relationship between the  
 280 mean area of features,  $A_m$ , and  $P_z$ . However, as shown in Figure 3a, there is also a strong  
 281 observed relationship in interannual variability between  $A_m$  and the total area coverage  
 282 of heavy precipitation,  $C$  [ $r^2(C, A_m) \sim 0.7$ ], with greater  $C$  favoring greater  $A_m$ . This  
 283 suggests a large part of the observed regression pattern is due to the effect of changes  
 284 in the total precipitating area, rather than a pure spatial redistribution of a fixed num-  
 285 ber of heavily precipitating points. This complicates the interpretation of increased clus-  
 286 tering in internal variability, since when comparing climates, the mean area coverage of  
 287 heavy precipitation  $\bar{C}$  remains fixed at 5%. To address this, we estimate the variations  
 288 in the distribution of heavy precipitation that contribute to variations in  $A_m$  indepen-  
 289 dent of changes in  $C$  using Pearson partial corelation (see Methods).

290  $P_z$ ,  $P_{eq}$  and  $P_{heq}$  are positively correlated with the mean area of heavy precipi-  
 291 tation features,  $A_m$ , when the effect of changes in the area coverage of heavy precipita-  
 292 tion,  $C$ , is removed (star in Figure 3b), suggesting that there is a shift of heavy rainfall  
 293 toward the equator and the central Pacific when the tropics are highly clustered. For a  
 294 given  $C$ , this contraction of heavily precipitating regions explains about 5-10 percent of  
 295 the remaining variance in  $A_m$  after the effect of changes in  $C$  is removed.

296 Both the CMIP ensemble and the high-resolution model generally show similar spa-  
 297 tial patterns associated with increasing large-scale clustering (Figure S4 in the support-  
 298 ing information). All models show significant relationships between  $A_m$  and  $C$ , although  
 299 on average somewhat weaker than in observations (Figure 3b), and most models show  
 300 significant positive partial correlations between the proximity metrics  $P_z$ ,  $P_{eq}$ , and  $P_{heq}$   
 301 with 24, 22, and 21 out of 27 CMIP6 models exhibiting statistically significant rela-  
 302 tionships after removing the effect of changes in  $C$ , respectively (Figure 4). That is, as for

303 the observations, most models agree that higher clustering, as measured by a larger mean  
304 area for a given area coverage of heavy precipitation features, is associated with a shift  
305 in heavy precipitation to the central equatorial Pacific. Interestingly, the high-resolution  
306 GCM did not show a significant partial correlation with  $P_{eq}$ , suggesting clustering in that  
307 model is not sensitive to the meridional contraction of heavy precipitation to the geo-  
308 graphic equator.

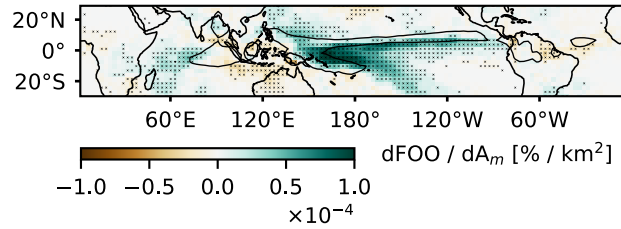


**Figure 2.** GPCP frequency of occurrence of heavy precipitation,  $FOO$ , regressed onto the mean area of heavy precipitation features,  $A_m$ , for interannual variability. The contour shows the 90th percentile of the climatological  $FOO$  and crosses indicate whether correlations are statistically significant.

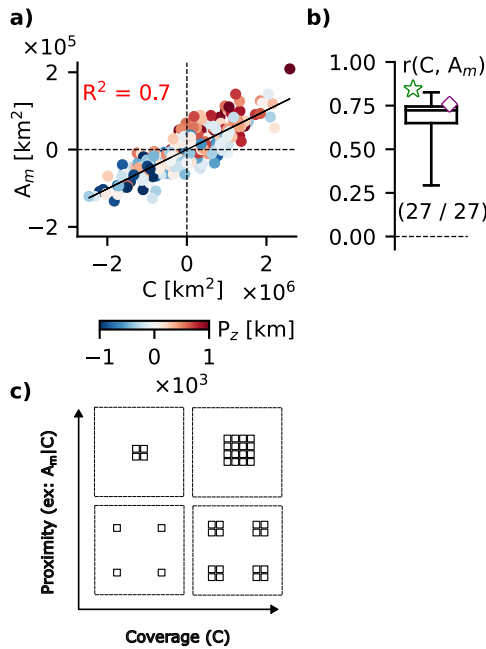


**Figure 3.** Scatter plot of monthly anomalies in area coverage of heavy precipitation,  $C$ , and the mean area of heavy precipitation features,  $A_m$ , colored by the zonal proximity of heavy precipitation to the longitude  $180^\circ E$  in the central pacific,  $P_z$ , for GPCP observations (a). Boxplot of the correlations between  $C$  and  $A_m$  for the CMIP6 ensemble (b). The fraction of CMIP models with statistically significant correlations is indicated below the box, and the GPCP (star) and high-resolution GCM (diamond) correlations are shown in lighter colors if not statistically significant. Schematic of the relationship between the number,  $N$ , and mean area of heavy precipitation features,  $A_m$ , and coverage of heavy precipitation,  $C$  (c).  $A_m$  increase from bottom left to top right panel,  $N$  decrease from bottom right to top left panel, and a spatial clustering in this framework is interpreted as increasing  $A_m$  for a given  $C$ , denoted  $A_m|C$ .

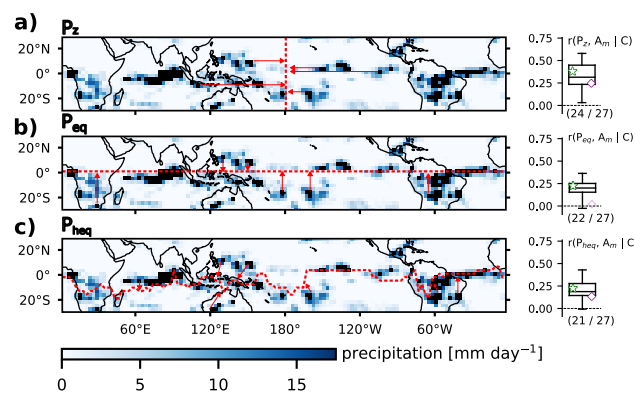


**Figure 4.** Schematic of metric and boxplot of its partial correlations with  $A_m$  outside the influence of  $C$ , for  $P_z$  (a),  $P_{eq}$  (b),  $P_{heq}$  (c) in the CMIP6 ensemble. The fraction of CMIP models with statistically significant correlations is indicated below each box, and the GPCP (star) and high-resolution GCM (diamond) correlations are shown in lighter colors if not statistically significant.

309 We now consider how large-scale clustering of heavy precipitation changes under  
 310 climate change. Bläckberg & Singh (2022) noted that large-scale clustering increases as  
 311 the climate warms in projections of climate change by the CMIP5 ensemble. Figure 5a  
 312 shows that this is also true for CMIP6; all models project an increase in  $A_m$  with warming  
 313 to varying degrees. However, there is a wide spread in climatological  $A_m$  and wide  
 314 spread in climatological increase in  $A_m$  across the ensemble, suggesting the degree of large-  
 315 scale clustering and the change in large-scale clustering with warming is poorly constrained  
 316 in the models.

317 Given the climatologically fixed  $C$  in this framework, changes in the mean area of  
 318 precipitation features,  $A_m$ , with warming are driven entirely by a spatial reorganization  
 319 of convection to larger features. The present analysis evaluates whether the spatial pat-  
 320 terns associated with a high degree of clustering of precipitation in interannual variabil-  
 321 ity may also be relevant to the redistribution of heavy precipitation due to the forced  
 322 response from global warming. Indeed, all but one model show an increase in  $P_{eq}$  with  
 323 warming, indicating a contraction of heavy precipitation towards the geographic equa-  
 324 tor (Figure 5b) and all models contract heavy precipitation towards the hydrological equa-  
 325 tor, or "ITCZ center". One possible interpretation of this is that a narrowing of the ITCZ  
 326 provides a mechanism for the overall increase in clustering with warming. However, we  
 327 note that the change in  $P_{eq}$  and  $P_{heq}$  with warming is uncorrelated with the change in  
 328  $A_m$  across the CMIP6 ensemble; models exhibiting stronger ITCZ narrowing with warm-  
 329 ing do not show stronger increases in large-scale clustering of precipitation. On the other  
 330 hand, there is a significant correlation between increases in mean area of precipitation  
 331 features,  $A_m$ , and changes in  $P_z$  across the CMIP6 ensemble. That is, models that show  
 332 a greater clustering with warming also show a zonally smaller expansion / greater con-  
 333 traction of heavy precipitation to/from the central Pacific (note that the zonal and merid-  
 334 ional contractions are somewhat anticorrelated, as also identified by Popp & Bony (2019)).  
 335

336 Going beyond the simple distance metrics, Figure 6 regresses the projected increase  
 337 in frequency of occurrence of heavy precipitation onto the projected increase in  $A_m$  across  
 338 the CMIP ensemble. This reveals a spatial pattern of precipitation changes with several  
 339 similarities to the pattern for interannual variability shown in Figure 2. However, an im-  
 340 portant distinction is that, for changes with warming, the redistribution of heavy pre-  
 341 cipitation is a conserved property, due to the climatologically fixed  $C$ . Similarities be-  
 342 tween the regression patterns include a regression coefficient largest in the central Pa-  
 343 cific close to the equator, and a redistribution of precipitation away from the maritime  
 344 continent, Amazon, and Atlantic. While under interannual variability heavy precipita-  
 345 tion shifts southward in the Pacific for highly clustered states, the changes with warm-  
 346 ing show a northward shift of heavy precipitation in the Pacific.  
 347

348 We note that the spatial patterns associated with a climatologically high degree  
 349 of clustering of heavy precipitation across the CMIP6 ensemble (Figure S5 in the sup-  
 350 porting information) are rather different from those of internal variability and changes  
 351 with warming . Models with high climatological values of  $A_m$  tend to have more con-  
 352 vection in the warm pool, over tropical continents, and at the edges of the northern and  
 353 southern convergence zones over the Pacific Ocean. These relationships cannot be sum-  
 354 marized by a single value of either  $P_z$ ,  $P_{eq}$ , or  $P_{heq}$ . Rather, we find that high climato-  
 355 logical values of  $A_m$  are associated with high month-to-month variability in  $C$ . This in-  
 356 dicates that high climatological clustering corresponds to high clustering in time, with  
 357 some days producing a large amount of heavy precipitation across the tropics and other  
 358 days producing much less.  
 359

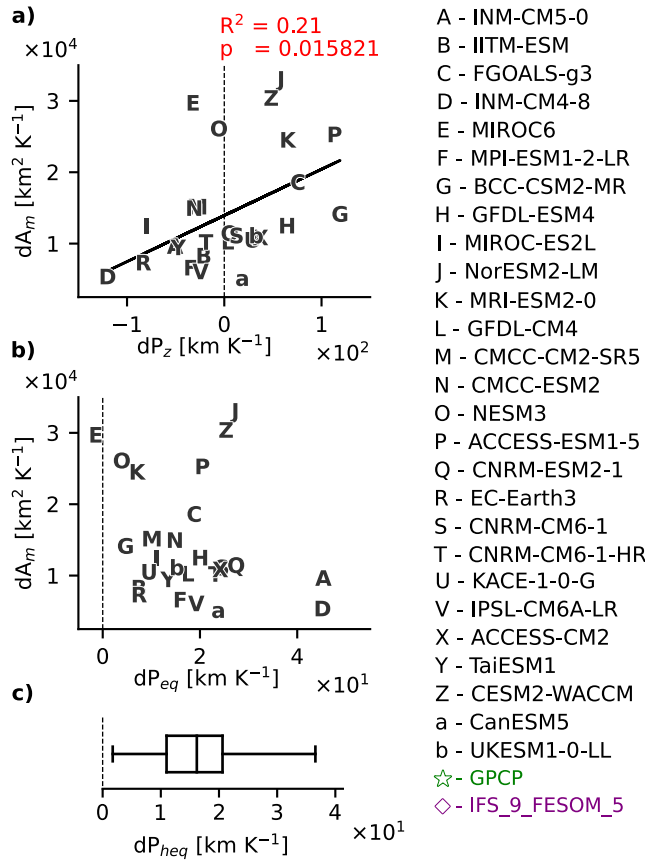


**Figure 5.** Scatter plot of change in climatological mean area of heavy precipitation features,  $A_m$ , with change in climatological mean distance of heavy precipitation to the central pacific,  $P_z$  (a) and change in mean heavy precipitation proximity to the geographic equator,  $P_{eq}$  (b). Boxplot of change in climatological mean distance to the hydrological equator,  $P_{heq}$  (c), where the hydrological equator is defined as the latitude of highest specific humidity at 700 hPa as a function of longitude and time in months. All quantities are normalized by the tropical surface temperature warming (land and ocean) from the historical to the SSP585 scenario simulation period in CMIP6 models.

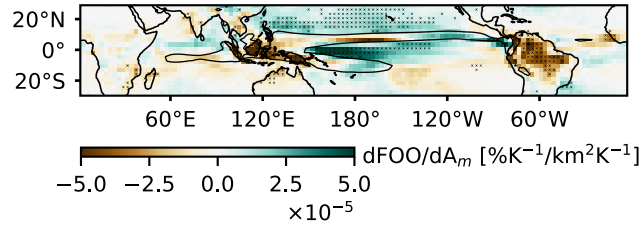


**Figure 6.** Increase in frequency of occurrence of heavy precipitation,  $FOO$ , regressed onto increase in  $A_m$  per kelvin tropical warming from the historical to the SSP585 scenario simulation period across the CMIP6 ensemble. Contour shows the ensemble-mean 90th percentile of  $FOO$  in the historical period and crosses indicate whether correlations are statistically significant.

In summary, the spatial patterns of heavy precipitation associated with highly clustered states vary across timescales, but there are important common threads. In both internal variability and for changes with warming, higher clustering as measured by  $A_m$  is associated with more heavy precipitation in the central equatorial Pacific. In particular, models with stronger increases in large-scale clustering of precipitation under warming also exhibit a relatively greater zonal shift in convection to the central Pacific. This potentially suggests the Walker circulation, and the East-West SST gradient in the Pacific, as an important control on the magnitude of changes in large-scale clustering of precipitation with warming. We next investigate the mechanisms associated with large-scale clustering, including SST changes, cloud-radiative feedbacks, and a “narrowing of the ITCZ” in both internal variability and under climate change.

## 368 4 Mechanisms associated with Heavy Rainfall Clustering

369 This section investigates the extent to which changes in the El Niño-Southern Os-  
 370 cillation (ENSO) can explain changes in clustering, discuss whether top of the atmosphere  
 371 radiative fluxes may positively feedback on the highly clustered states, and if a merid-  
 372 ional clustering of heavy rainfall with warming is related to constraints on the tropical  
 373 ascent area fraction.

374 We use the Southern Oscillation Index (SOI; Ropelewski & Jones, 1987) and the  
 375 Oceanic Niño Index (ONI; Sobel et al., 2002) to identify the state of the El Niño-Southern  
 376 Oscillation in interannual variability and compare ascent area fraction,  $A_a$ , using the area  
 377 where the 500 hPa vertical pressure velocity is negative. The SOI represents the stan-  
 378 dardized deseasonalized monthly anomalies of the surface pressure difference between  
 379 Tahiti (17.6°S, 149.6°W) and Darwin (12.5°S, 130.9°E), calculated here as the three-  
 380 month rolling average. The ONI represents the three-month rolling average SST anomaly  
 381 in the Niño3.4 region (5°S- 5°N, 120°-170°W), calculated here relative to the full range  
 382 of years used in the climatology. SOI (ONI) values less (greater) than -7 (0.5) repre-  
 383 sent El Niño conditions and SOI (ONI) values greater (less) than 7 (-0.5) represent La  
 384 Niña conditions. The climatological East-West Pacific SST gradient, defined as the time-  
 385 mean difference between the SST in the western- (5°S - 5°N, 80° - 150E) and eastern  
 386 (5°S - 5°N, 180° - 80°W) Pacific boxes, which we denote  $T_z$ , serves as an indicator for  
 387 climatologically “El Niño-like” conditions (Watanabe et al., 2024).

388 Observations show several indications that highly clustered states, corresponding  
 389 to large values of the mean area of heavy precipitation features,  $A_m$ , are associated with  
 390 El Niño-like conditions in interannual variability. Firstly, surface temperature regressed  
 391 onto  $A_m$  shows a pattern strongly reminiscent of an El Niño SST signature (Alexander  
 392 et al., 2002) (Figure 7). Secondly, during times of ONI exceeding 0.5°C compared to all  
 393 days,  $A_m$  increases as heavy precipitation moves from the maritime continent towards  
 394 the central Pacific (Figure S6 in supporting information). Finally, in absolute value and  
 395 independent of changes in  $C$ , SOI and ONI show a negative (positive) correlation with  
 396  $A_m$  (Figure 8a and Figure S1 in supporting information). From qualitatively analysing  
 397 snapshots of observed precipitation features from the climatology of individual months  
 398 during El Niño and La Niña conditions (interannual variability), a greater mean area of  
 399 heavy rainfall is favoured during El Niño conditions due to a greater total area cover-  
 400 age of heavy precipitation locally growing precipitation features in combination with more  
 401 frequently forming large connected components (precipitation features) in the central Pa-  
 402 cific (ex: Figure 1c). From these results, we may argue ENSO as a driver for interan-  
 403 nual variability in clustering, however, it is possible that radiative effects associated with  
 404 clustering may feedback on its development and maintenance. Initial investigation sug-  
 405 gest such radiative feedbacks are present and may contribute to amplifying the existing  
 406 pattern of the frequency of occurrence of heavy precipitation associated with the highly  
 407 clustered states (Figure S7 in supporting information).

408 Most CMIP models capture the observed connection between SOI and  $A_m$  (Fig-  
 409 ure S1 in the supporting information) and the independent contribution of SOI on  $A_m$   
 410 outside the influence of  $C$ , as does the high-resolution GCM (Figure 8b). Thus both mod-  
 411 els and observations show that large-scale clustering of precipitation is greater during  
 412 El Niño than La Niña in interannual variability. This is despite the fact that El Niño rep-  
 413 presents a weakening of the Walker circulation and a weakening of tropical SST gradients,  
 414 both of which are generally thought to facilitate the organization of convection on large  
 415 scales.

416 The interpretation as to whether large-scale clustering is favoured during El Niño  
 417 events will be sensitive to whether clustering is interpreted as increasing or decreasing  
 418 with total area coverage of heavy precipitation,  $C$ , for example when using  $N$  instead  
 419 of  $A_m$ , and may be sensitive to the temporal and spatial resolution of the precipitation

dataset as well as the clustering metric used. Notably, from idealized SST perturbed GCM experiments Quan et al. in 2025 find "La Niña" like conditions favour highly clustered states on the large scale, but target increases in "unevenness", or precipitation gradients, as large-scale clustering (GINI index). Still, in observed and modelled interannual variability in the present study the GINI index is somewhat negatively correlated with SOI ( $r \sim -0.15$  -  $-0.4$ ), indicating more El Niño like conditions favour highly clustered states (Figure S1 in supporting information). We suspect the diverging results is due to how the ENSO related SST pattern manifest naturally compared to when experimentally imposed, for example including a "horseshoe" shaped relative cooling in the Pacific in natural variability during El Niño events. However, this interpretation is tentative and requires further investigation.

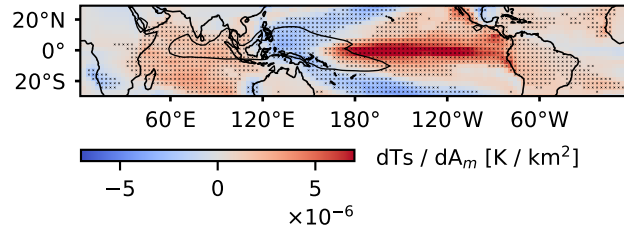


**Figure 7.** NOAA-GlobalTemp surface temperature (land and ocean),  $T_s$ , regressed onto  $A_m$  for interannual variability. The contour shows the climatological 90th percentile of  $T_s$ , and crosses indicate whether correlations are statistically significant.

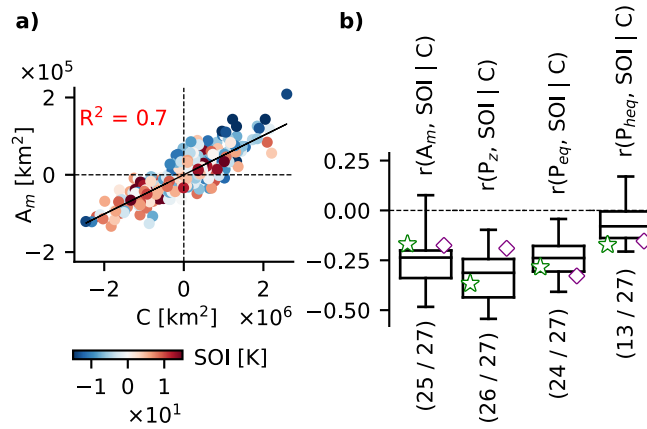


**Figure 8.** Same as Figure 3, but with the Southern Oscillation Index (SOI) in scatter colors and as explanatory variable in boxplot.

431        The strong connection between El Niño conditions and clustering in interannual  
432        variability motivates the investigation of changes in the climatological Pacific SST gra-  
433        dient to a more El Niño-like state as a mechanism for explaining model-spread in pro-  
434        jected changes in clustering. Consistent with expectations, the magnitude of the weak-  
435        ening of the East-West Pacific SST gradient explains a similar amount of variance in pro-  
436        jected changes in clustering as the zonal shift in heavy precipitation (Figure 9). Mod-  
437        els that have more El Niño-like warming patterns tend to exhibit larger increases in large-  
438        scale clustering of precipitation. Regressing the SST changes against projected changes  
439        in the mean area of precipitation features,  $A_m$ , also shows an El-Niño-like pattern, with  
440        a relative warming in the east and relative cooling in the west (Figure 10). In addition,  
441        the regression pattern has a noticeable north-south gradient, consistent with the pos-  
442        itive regression coefficients for heavy precipitation frequency north of the equator in Fig-  
443        ure 6.

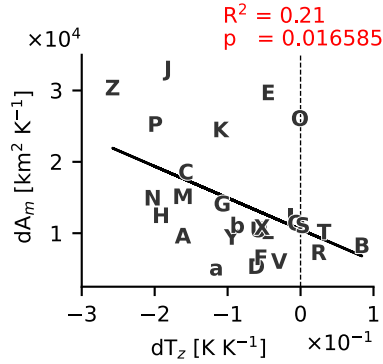


**Figure 9.** Same as Figure 4a, but with the change in the climatological Pacific SST gradient,  $T_z$ , per Kelvin tropical warming from the historical to the SSP585 scenario simulation period across the CMIP6 ensemble as explanatory variable. Models are as given in the legend in Figure 4.

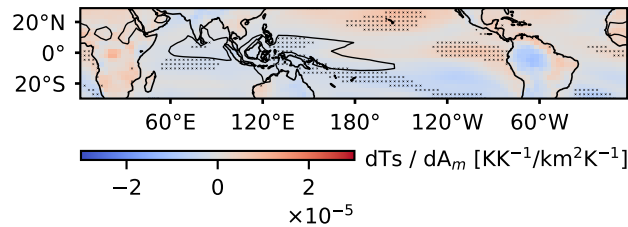


**Figure 10.** Change in surface temperature,  $T_s$ , regressed onto change in mean area of heavy precipitation features,  $A_m$ , per Kelvin tropical warming from the historical to the SSP585 scenario simulation period across the CMIP6 ensemble. Contour shows ensemble-mean 90th percentile climatological  $T_s$  and crosses indicate if correlations are statistically significant.

444 Note, while changes to the Pacific SST gradient may be climatologically argued as  
445 a driver for changes in clustering with warming there are changes in the zonal SST gra-  
446 dient,  $T_z$ , and the mean distance of heavy precipitation to the central Pacific of both signs  
447 across the 27 CMIP6 models we analyse, suggesting that zonal shifts in convection are  
448 not the primary reason for the ensemble-mean increase in large-scale clustering with warm-  
449 ing that we document. We hypothesize that the ensemble-mean increase in  $A_m$  is instead  
450 associated with a meridional shift in convection. All but one model increase proximity  
451 of heavy precipitation to the geographic and hydrological equator with warming, and this  
452 is associated with an increase in the large-scale clustering of precipitation in natural vari-  
453 ability. The increased proximity of heavy precipitation to the hydrological equator with  
454 warming can be interpreted as a meridional clustering of convection to the centre of the  
455 ITCZ, or a “narrowing” of the ITCZ. Mechanistically, changes to the “width” or area  
456 of the ITCZ characterized by changes in the tropical ascent area fraction relative to de-  
457 scent area fraction is theorized to be controlled by convective limitations on the efficiency  
458 of moisture and heat export from the ITCZ to its surroundings (the Gross Moist Sta-  
459 bility) (Byrne & Schneider, 2016). From this framework, the forced response to global  
460 warming modulate the “width” (or area) of the ITCZ to maintain the energy balance  
461 between regions of ascent and descent. While the narrowing tendency is a combination  
462 of ascent area reduction and descent area expansion, a reasonably strong relationship  
463 between ascent area fraction,  $A_a$ , and proximity of heavy rainfall to the hydrological equa-  
464 tor,  $P_{heq}$ , (Figure 11) support the notion of a mechanistic connection to aspects of large-  
465 scale clustering of heavy precipitation.

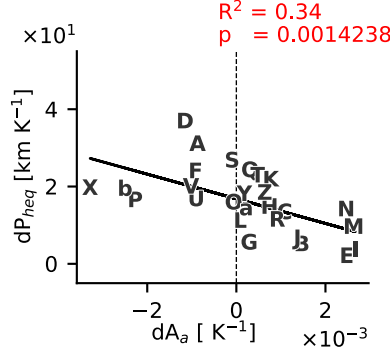


**Figure 11.** Same as Figure 4a, but with the change in climatological area of ascent,  $A_a$ , per Kelvin tropical warming from the historical to the SSP585 scenario simulation period across the CMIP6 ensemble as explanatory variable. Here, the climatological area of ascent is calculated as the climatological time-mean of the fraction of the tropical domain where the monthly-mean 500hpa vertical pressure velocity in negative. Models are as given in the legend in Figure 4.

In this section we have shown that El Niño-like states tend to result in a higher degree of clustering in both interannual variability and across the CMIP6 ensemble under climate change, but highlight cloud-radiative feedbacks and energetic constraints on the large-scale circulation of moisture and heat (Byrne & Schneider, 2016) may influence the manifestation of clustering in interannual variability and for climatological changes with warming, respectively. In the next section, we explore the tropical humidity and cloud distributions associated with clustered states and how it relates to climate sensitivity.

## 473 5 Heavy Rainfall Clustering and Radiative feedbacks associated with 474 Climate Sensitivity

475 We now consider how large-scale clustering of precipitation influences the cloud and  
476 humidity distribution. Our motivation is to understand how such clustering may con-  
477 nect to radiative feedbacks. Previous authors have found that the degree of clustering  
478 on different spatial scales has an effect on the radiation budget and clouds (e.g., Bony  
479 et al., 2020; Wing & Emanuel, 2014; Pendergrass et al., 2016). The literature suggests  
480 changes in clustering under warming may lead to different cloud feedbacks and may there-  
481 fore affect equilibrium climate sensitivity (ECS) (Schiro et al., 2022). This section in-  
482 vestigates this hypothesis for large-scale clustering across the CMIP6 ensemble. As for  
483 previous sections, the analysis assesses whether relationships in interannual variability  
484 can be used to infer the response to climate change, raising the possibility of an obser-  
485 vational constraint on particular radiative feedbacks or ECS itself.

486 Rather than focusing on changes in radiative fluxes or calculating feedback strength  
487 directly, we focus on changes in mid-tropospheric relative humidity, which has been ar-  
488 gued to cause a negative longwave feedback associated with changes in convective or-  
489 ganization (Tobin et al., 2013; Bony et al., 2020), and changes in low-cloud fraction in  
490 regions of subsidence, which have been argued to cause a positive shortwave feedback  
491 associated with changes in convective organization (Schiro et al., 2022). Changes in low  
492 clouds in regions of subsidence are also known to be important for understanding model  
493 spread in ECS (Zelinka et al., 2020). Correlations between measures of large-scale clus-  
494 tering of heavy precipitation and various other metrics commonly used to assess changes  
495 to the radiation budget on interannual and climatological timescales are presented in Fig-  
496 ure S1-2 in the supporting information.

497 For our analysis, the mid-tropospheric relative humidity, RH, is taken as the 500  
498 hPa value. Observed low-cloud fraction, LCF, is calculated using the ISCCP weather  
499 states (Tselioudis et al., 2010) as described in Section 2.2, and taken as the cloud frac-  
500 tion below 600 hPa. CMIP6 low-cloud fraction is calculated analogously, with cloud frac-  
501 tion pre-processed by interpolating hybrid-sigma coordinates to 19 pressure levels if not  
502 already available on pressure levels. We also consider the mean low-cloud fraction in re-  
503 gions of descent, denoted by a subscript  $d$  and calculated as the tropical-mean of grid-  
504 points for which the monthly-mean vertical pressure velocity at 500 hPa is positive. Later  
505 we will consider variables in regions of ascent, defined analogously for negative 500 hPa  
506 vertical velocity and identified by a subscript  $a$ .

507 Figure 12a and Figure 13a show observational estimates of the regression patterns  
508 of RH and LCF against the mean area of precipitation features,  $A_m$ , for interannual vari-  
509 ability. The regressions show a clear El-Niño-like pattern, with increases in RH and de-  
510 creases in LCF in the central and eastern Pacific, and opposite changes over the warm  
511 pool. This suggests the changes in RH and low clouds with increased tropical cluster-  
512 ing are caused at least in part by variations associated with El Niño-Southern Oscilla-  
513 tion.

514 From a tropics-wide perspective, when the observed degree of clustering is high ac-  
515 cording to  $A_m$ , the tropical mean is drier (Figure 12b) while LCF increases, both when  
516 averaged over descending grid points ( $LCF_d$  in Figure 13b) and in regions of time-mean  
517 descent (contour on Figure 13a). The environmental signature associated with large-scale  
518 clustering is therefore consistent with a negative longwave feedback identified for large-  
519 scale clustering in idealized simulations (Arnold & Randall, 2015) and a longwave- and  
520 low-cloud cooling signature found associated with interannual variations in mesoscale or-  
521 ganization in observations (Bony et al., 2020). However, partial correlations of  $A_m$  with  
522 RH excluding the influence of the total area coverage of heavy precipitation,  $C$ , are in-  
523 significant in the observations (Figure 12b). This suggests that the influence of  $A_m$  on  
524 relative humidity is almost entirely due to increasing  $C$ . Observed correlations of rela-

525 tive humidity and the distance metrics  $P_{eq}$ ,  $P_{heq}$  and  $P_z$ , representing proximity of heavy  
 526 rainfall to the equator and the central Pacific, respectively, are also generally insignif-  
 527 icant. Observed  $LCF_d$  on the other hand increases for all three forms of spatial cluster-  
 528 ing, outside the influence of  $C$  (Figure 13b).

529 The CMIP6 ensemble generally agrees on the strong association between  $C$  and the  
 530 aforementioned tropical environmental signatures. However, unlike the observational es-  
 531 timates, about half of the models also show a significant relationship between relative  
 532 humidity and spatial shifts of heavy precipitation (Figure 12b). In particular, in a sub-  
 533 set of models, zonal shifts in heavy precipitation to the central Pacific are (independent  
 534 of variations in  $C$ ) associated with a moistening in the tropics, while meridional shifts  
 535 to the equator result in domain-mean drying. These relationships are also present in the  
 536 high-resolution GCM. The models generally do not capture the observed  $LCF_d$  signa-  
 537 ture for clustering outside the influence of  $C$ , except for a subset of CMIP models pro-  
 538 ducing increases in  $LCF_d$  for meridional shifts in heavy precipitation (Figure 13b). Other  
 539 notable independent effects of the spatial preference of heavy precipitation on environ-  
 540 mental conditions include a reduction in high cloud fraction above 400 hPa in regions  
 541 of ascent,  $HCF_a$ , with observed and modelled meridional shifts in precipitation ( $r(P_{eq}, HCF_a | A_f) \sim$   
 542 0.25).

543 Our analysis of interannual variability has revealed strong relationships between  
 544 RH and low-cloud fraction and large-scale clustering of precipitation in observations. How-  
 545 ever, in observations, the RH relationships are primarily driven by changes in the to-  
 546 tal area coverage of heavy precipitation,  $C$ .  $C$  also influences low cloud fraction,  $LCF_d$ ,  
 547 but spatial shifts in heavy precipitation retains a connection to  $LCF_d$  outside the influ-  
 548 ence of  $C$  in observations.

549 While  $C$  is primarily viewed in this framework as a confounding variable, to com-  
 550 pare interannual variability in an analogous way to climatological changes with warm-  
 551 ing, we find some limitations of this method. While  $C$  is largely controlled by the tropical-  
 552 mean rainfall rate for the 90th, 95th, and 97th percentile, the area covered by the 95th  
 553 percentile heavy rainfall rate is partly a function of the spatial clustering of the 90th per-  
 554 centile rainfall and, when using the 90th percentile threshold, changes in  $A_m$  for a given  
 555  $C$  is correlated with tropical-mean relative humidity instead of  $C$ . The sensitivity to the  
 556 percentile threshold in the relationships presented in this section is only true for inter-  
 557 annual variability in relative humidity and  $A_m$  changes independent of  $C$ . We now con-  
 558 sider relationships between RH and low-cloud fraction changes and changes in the clus-  
 559 tering of precipitation in climate projections.

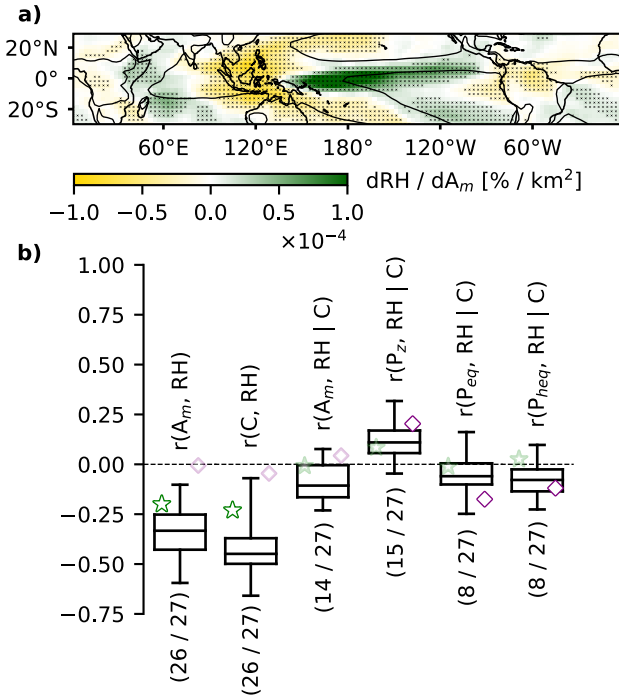


**Figure 12.** Relative humidity at 500 hPa, RH, regressed onto mean area of heavy precipitation features,  $A_m$ , in interannual variability (a). Boxplots of correlations and partial correlations outside the influence of the total area coverage of heavy precipitation,  $C$ , of RH and  $A_m$ , mean distance of heavy precipitation to 180°E,  $P_z$ , and mean distance of heavy precipitation to the geographic and hydrological equator,  $P_{eq}$  and  $P_{heq}$  (b). Star and diamond show results for observations and high-resolution GCM, respectively, shown in lighter colors if not statistically significant. The numbers below the boxplots gives the fraction of models with statistically significant correlations.

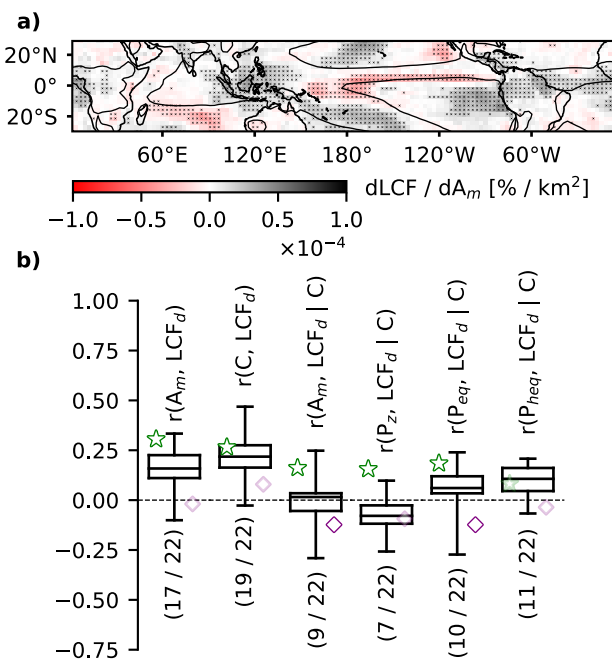


**Figure 13.** Same as Figure 12, but with the low cloud fraction, LCF, and low cloud fraction in regions of descent,  $\text{LCF}_d$ , as response variable.

560 Consistent with the results from the previous section, models with larger increases  
 561 in large-scale clustering under warming tend to have changes in relative humidity and  
 562 clouds consistent with an El Niño-like shift in the tropical circulation. The regression  
 563 patterns of RH and LCF onto changes in  $A_m$  under warming across the CMIP6 ensemble  
 564 (Figure S8a-b) are similar to those for interannual variability presented above. How-  
 565 ever, in contrast to the case for interannual variability, changes in overall clustering ac-  
 566 cording to  $A_m$  with warming have little connection to changes in tropical-mean mean  
 567 RH or low-cloud fraction in regions of descent,  $LCF_d$ , across the CMIP6 ensemble (Fig-  
 568 ure 14a, b). Given this, it is perhaps not surprising that there is no correlation between  
 569 the increase in  $A_m$  within a model under warming and the model's ECS (Figure 14c).  
 570 Here we take ECS from the supplementary material of Zelinka et al. (2020) and Haus-  
 571 father et al. (2022).

572 The results therefore indicate that changes in a general clustering of heavy precip-  
 573 itation features,  $A_m$ , under warming do not strongly affect radiative feedbacks, despite  
 574 indications from observations that more clustered states in this way are drier with more  
 575 low-clouds in regions of large-scale descent. One reason for this result appears to be the  
 576 different ways in which large-scale clustering of heavy rainfall can manifest at different  
 577 timescales. In interannual variability, increases in heavy precipitation clustering are as-  
 578 sociated with increases in the total area coverage of heavy precipitation, defined here  
 579 by  $C$ . Under climate change, increases in  $C$  in one month must be balanced by decreases  
 580 in another month such that the overall average must remain constant. When the effects  
 581 of changes in total area coverage are removed, the observed relationship to RH becomes  
 582 weak. However, this explanation is not the whole story, as many of the models do ex-  
 583 hibit changes in RH associated with increased clustering independent of changes in the  
 584 total area coverage of heavy precipitation. Even among this subset of models, however,  
 585 future increases in  $A_m$  are not a good predictor of future changes in clouds or relative  
 586 humidity. This suggests that caution should be used in extrapolating relationships—either  
 587 observed or simulated—between large-scale clustering and other properties of the climate  
 588 in internal variability to those for climate change.

589 Finally, we note that there does exist a relationship between a tropical-mean dry-  
 590 ing and LCF in some key subsidence regions with the proximity of heavy rainfall to the  
 591 geographic and hydrological equator (Figure S2 and S8g-h in supporting information).  
 592 Under warming, variations in the meridional contraction of heavy rainfall, as measured  
 593 by the mean distance of heavily precipitating gridpoints to the equator  $P_{eq}$ , explain about  
 594 45 percent of the variance in tropical-mean drying (Figure 16 and Figure 15). This re-  
 595 lationship is consistent with the sign of the relationship between RH and  $P_{eq}$  in inter-  
 596 annual variability in a subset of CMIP6 models (Figure 12b). This result potentially high-  
 597 lights the importance of ITCZ narrowing as a specific manifestation of large-scale clus-  
 598 tering that appears to be important for setting the tropical-mean relative humidity. How-  
 599 ever, we note that most of the spread in projected drying is due to the result of four mod-  
 600 els with dramatically different drying trends. When these 4 models are removed from  
 601 the ensemble, the correlation is no longer present. Thus further work is required to con-  
 602 firm if this relationship is robust and physical.

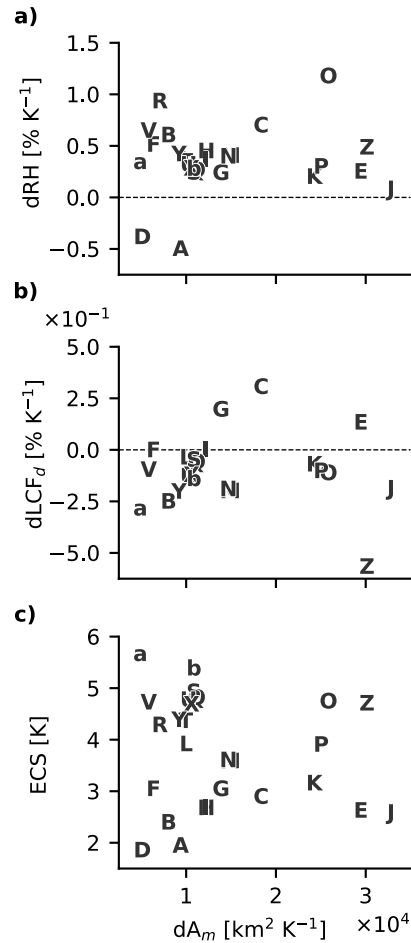


**Figure 14.** Scatter plot of change in  $A_m$  between historical period and SSP585 period per Kelvin tropical warming and associated tropical-mean change in 500 hPa relative humidity, RH, (a), low cloud fraction in regions of descent,  $LCF_d$  (b), and equilibrium climate sensitivity (ECS) in the CMIP6 ensemble (c). Models are as given in the legend in Figure 4.

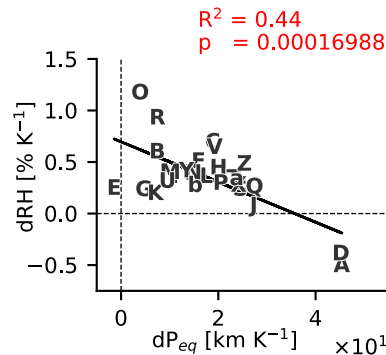


**Figure 15.** Scatter plot of change in mean distance of heavy precipitation to the geographic equator,  $P_{eq}$ , between historical period and SSP585 period per Kelvin tropical warming and associated tropical-mean change in 500hPa relative humidity, RH. Models are as given in the legend in Figure 4.

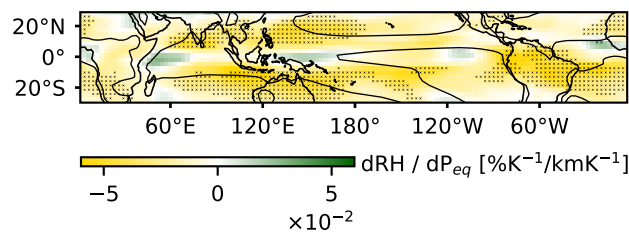


**Figure 16.** Change in relative humidity at 500 hPa, RH, regressed onto changes in mean distance of heavy precipitation to the geographic equator,  $P_{eq}$ , between the historical and SSP585 periods per Kelvin warming.

## 603    6 Summary and Discussion

604    In this paper we have (1) presented the dominant spatial patterns of heavy pre-  
 605    cipitation that produce a high degree of clustering on the large scale (Section 3); (2) tied  
 606    the associated spatial patterns to mechanisms associated with clustering through large-  
 607    scale SST patterns, cloud-radiative feedbacks, and area of ascent (Section 4); and (3) eval-  
 608    uated the associated changes in properties of the atmosphere that are important for the  
 609    radiation budget (Section 5) in both interannual variability and for projected changes  
 610    with warming. We have defined the degree of clustering of precipitation based on the  
 611    spatial distribution of the top 5 percent heaviest daily rainfall instances, with high gen-  
 612    eral clustering corresponding to scenes in which the mean area of individual precipita-  
 613    tion features is large. A challenge in any definition of convective organization is in how  
 614    one measures organization consistently as the total amount of precipitation changes (Retsch  
 615    et al., 2020; Tobin et al., 2013). In the present study, the use of a percentile precipita-  
 616    tion threshold accounts for changing mean precipitation rates in different climates. How-  
 617    ever, in internal variability, the mean area of precipitation features is affected by both  
 618    spatial shifts in the precipitation distribution and variations in the total area coverage  
 619    of heavy precipitation,  $C$ . This is addressed here by using Pearson partial correlations  
 620    to evaluate the independent contributions of different measures of the spatial distribu-  
 621    tion of precipitation while controlling for the effect of  $C$ .

622    When tropical precipitation is observed to be highly clustered on the large scale  
 623    in interannual variability, heavy precipitation gravitates meridionally to the equator and  
 624    zonally towards the central Pacific. In climate projections, large-scale clustering of pre-  
 625    cipitation is found to increase in all models, and this coincides with a shift of precipi-  
 626    tation toward the equator, across the ensemble. We therefore hypothesize that a nar-  
 627    rowing of the ITCZ, negatively correlated with climatological area of ascent,  $A_a$ , ( $r=-$   
 628    0.34) may be an important contributor to increases in large-scale clustering of precipi-  
 629    tation under warming. This implicates mechanisms related to the limitations of the trans-  
 630    port of energy by the Hadley circulation that have been argued to control changes in ITCZ  
 631    width as a forced response to global warming (Byrne & Schneider, 2016).

632    On the other hand, the intermodel spread in changes in clustering with warming  
 633    across the CMIP6 ensemble is related to zonal rather than meridional shifts in the pre-  
 634    cipitation. This motivated an investigation of the role played by Pacific SST gradients  
 635    in changes in large-scale clustering of precipitation. In interannual variability, El Niño-  
 636    Southern Oscillation linked variability appears to be a major driver of variability in large-  
 637    scale clustering of precipitation, with precipitation during El Niño events more clustered  
 638    than during La Niña events. However, there is indication that observed highly clustered  
 639    states may further involve cloud-radiative feedbacks on its development and/or main-  
 640    tenance.

641    Under warming, changes in zonal SST gradients appeared to explain the sensitiv-  
 642    ity of projected clustering to zonal shifts in heavy rainfall; those models with more El  
 643    Niño-like warming patterns tended to exhibit stronger increases in precipitation cluster-  
 644    ing. This is important given the large disagreement between observed and simulated SST  
 645    trends in the topical Pacific (e.g., Wills et al., 2022). Observations show a strengthen-  
 646    ing of the SST gradient, suggesting a weaker increase in large-scale clustering compared  
 647    to simulations, which tend to show a weakening of tropical SST gradients.

648    Finally, we assessed if the changes in clustering with warming may have an influ-  
 649    ence on climate sensitivity. In observed interannual variability, a greater area coverage  
 650    of heavy precipitation,  $C$ , is associated with a drier domain-mean and an increase in low-  
 651    cloudiness in subsidence regions,  $LCF_d$ . The connection between clustering for a given  
 652     $C$  persists for  $LCF_d$ , but changes in the mean area of precipitation features and merid-  
 653    ional and zonal shifts in heavy precipitation generally have weak relationships to the tropical-  
 654    mean relative humidity, RH, independent of their relationship to  $C$ .

GCMs from the CMIP ensemble generally capture the observed tropical environment signatures associated with changes in  $C$ , but often have different RH and LCF<sub>d</sub> connections to shifts in heavy precipitation independent of  $C$ . In contrast to observations, RH in several models is sensitive to both meridional and zonal shifts in heavy precipitation. In CMIP6 models, zonal shifts of precipitation to the central Pacific is associated with a more moist environment, whereas meridional shifts to the equator is associated with a drier environment. Realistically represented or not, these sensitivities appear to affect how these models project relative humidity into the future; the subset of models sensitive to drying from meridional contraction of heavy precipitation create considerable spread in the model ensemble relative humidity changes under warming ( $r=0.44$ ).

The study includes several limitations that are worth highlighting. Perhaps most importantly, the models we examined do not resolve the processes leading to organization of convection on mesoscales, which in turn may affect how they simulate heavy precipitation associated with large-scale convective features (Bao et al., 2017). This includes the high-resolution GCM, which still employs a parameterized convection scheme (Koldunov et al., 2023). Another limitation is the specific control applied as an energetic constraint across climates and confounding variable for interannual variability. Here we have used the total area covered by the 95th percentile threshold to represent heavy precipitation, which is largely set by the tropical-mean rainfall rate. However, between datasets, climates, seasons, and regions these precipitation thresholds may have differences in the convective features represented and therefore mechanisms that change its heavy rainfall and associated environment. Finally, we note that our model ensemble is one of opportunity, and the models and temporal- and spatial resolution of variables used were dictated by the available data. Correlation across the ensemble is not guaranteed to be produced by a physical relationship, and the extent to which such relationships arise by chance rise the more variables are examined. Nevertheless, the relationships between SST gradients and shifts in the precipitation distribution we highlight here are based on well-established physical relationships that provides some confidence in their robustness.

Future research is encouraged to adopt the isolation of total area coverage of convection, or other similar controls for changes in the mean precipitation rate, as used in the present framework. One avenue for further investigation is to identify models with realistic clustering compared to observations. The CMIP6 models considered here show a wide range in climatological clustering and internal variability in clustering, and perhaps a subset of models with more realistic clustering characteristics should be given more weight in projections of climate. In a similar way, investigating the connection between large-scale clustering and mesoscale clustering in high-resolution observations and storm resolving models may further constrain the model spread in projections by identifying unrealistic behavior. Further developing these research endeavors allow for increased confidence and reduce the model uncertainty in aspects of projections that could be influenced by changes in convective organization, ultimately allowing for improvement in mitigation and adaptation strategies for a warming climate.

**697 Open Research Section**

698 CMIP models used in this study are listed in Table S1 and model output is avail-  
699 able through the Earth System Grid Federation (ESGF) at <https://esgf-node.llnl.gov/search/cmip6/>.  
700 Observational datasets and access are listed here; GPCP precipitation dataset: <https://doi.org/10.5065/ZGJD-9B02>, ERA5 dataset: <https://doi.org/10.24381/cds.adbb2d47>, NOAA surface temper-  
701 ature dataset: <https://psl.noaa.gov/data/gridded/>, CERES outgoing longwave radia-  
702 tion dataset: <https://ceres.larc.nasa.gov/data/>, ISCCP: ISCCP cloud states dataset: <https://isccp.giss.nasa.gov/a>  
703 The IFS\_9\_FESOM\_5 model data is available via the World Data Center for Climate (WDCC)  
704 at DKRZ: [https://doi.org/10.26050/WDCC/nextGEMS\\_cyc2](https://doi.org/10.26050/WDCC/nextGEMS_cyc2). Code examples for repro-  
705 ducing key metric calculations and figures are available at Blackberg (2025a). Key met-  
706 rics are available at Blackberg (2025b).  
707

**Acknowledgments**

We acknowledge the World Climate Research Programme's Working Group on Coupled Modelling, which is responsible for CMIP, and we thank the climate modeling groups (listed in Table S1 in the supporting information) for producing and making available their model output. Further, we acknowledge the Deutsches Klimarechenzentrum (DKRZ) for providing resources for using the Levante supercomputer, which facilitated the analysis of the nextGEMS Cycle 2 simulation: IFS\_9\_FESOM\_5 used in this study. We also extend a special thank you to Dr. Cathy Hohenegger at Max Planck Institute for Meteorology for hosting the first author during a research visit to Hamburg, for providing guidance on model selection, and for facilitating access to institutional resources that greatly supported the analysis of the high-resolution GCM used in this study. Finally, we acknowledge support from the Australian Research Council (ARC) (grant no. DP230102077), the ARC Centre of Excellence for the Weather of the 21st Century (grant no. CE170100023), and computational resources and services from the National Computational Infrastructure, all funded by the Australian Government.

723 **References**

- Alexander, M. A., Bladé, I., Newman, M., Lanzante, J. R., Lau, N.-C., & Scott, J. D. (2002). The atmospheric bridge: The influence of enso teleconnections on air-sea interaction over the global oceans. *Journal of Climate*, 15(16), 2205 - 2231. Retrieved from [https://journals.ametsoc.org/view/journals/clim/15/16/1520-0442.2002.015.2205.tabtio\\_2.0.co\\_2.xml](https://journals.ametsoc.org/view/journals/clim/15/16/1520-0442.2002.015.2205.tabtio_2.0.co_2.xml) doi: 10.1175/1520-0442(2002)015<2205:TABTIO>2.0.CO;2
- Arnold, N. P., & Randall, D. A. (2015). Global-scale convective aggregation: Implications for the madden-julian oscillation. *Journal of Advances in Modeling Earth Systems*, 7(4), 1499-1518. Retrieved from <https://agupubs.onlinelibrary.wiley.com/doi/abs/10.1002/2015MS000498> doi: <https://doi.org/10.1002/2015MS000498>
- Bao, J., Sherwood, S. C., Colin, M., & Dixit, V. (2017, 10). The robust relationship between extreme precipitation and convective organization in idealized numerical modeling simulations. *Journal of Advances in Modeling Earth Systems*, 9, 2291-2303. Retrieved from <https://agupubs.onlinelibrary.wiley.com/doi/full/10.1002/2017MS001125> doi: 10.1002/2017MS001125
- Blackberg, P. (2025a). *Large-scale clustering of tropical precipitation: Code repository*. Zenodo. Retrieved from <https://doi.org/10.5281/zenodo.17070290> ([Software]) doi: 10.5281/zenodo.17070290
- Blackberg, P. (2025b). *Metrics for large-scale clustering of tropical precipitation*. Zenodo. Retrieved from <https://doi.org/10.5281/zenodo.16946243> ([Dataset]) doi: 10.5281/zenodo.16946243
- Bläckberg, C. P., & Singh, M. S. (2022, 5). Increased large-scale convective aggregation in cmip5 projections: Implications for tropical precipitation extremes. *Geophysical Research Letters*, 49. Retrieved from <https://agupubs.onlinelibrary.wiley.com/doi/full/10.1029/2021GL097295> doi: 10.1029/2021GL097295
- Bony, S., Semie, A., Kramer, R. J., Soden, B., Tompkins, A. M., & Emanuel, K. A. (2020). Observed modulation of the tropical radiation budget by deep convective organization and lower-tropospheric stability. *AGU Advances*, 1(3), e2019AV000155. Retrieved from <https://agupubs.onlinelibrary.wiley.com/doi/abs/10.1029/2019AV000155> (e2019AV000155 10.1029/2019AV000155) doi: <https://doi.org/10.1029/2019AV000155>
- Bretherton, C. S., Blossey, P. N., & Khairoutdinov, M. (2005, December). An energy-balance analysis of deep convective self-aggregation above uniform sst. *Journal of the Atmospheric Sciences*, 62(12), 4273-4292. Retrieved from <http://dx.doi.org/10.1175/JAS3614.1> doi: 10.1175/jas3614.1
- Byrne, M. P., & Schneider, T. (2016). Energetic constraints on the width of the intertropical convergence zone. *Journal of Climate*, 29(13), 4709 - 4721. Retrieved from <https://journals.ametsoc.org/view/journals/clim/29/13/jcli-d-15-0767.1.xml> doi: 10.1175/JCLI-D-15-0767.1
- Doelling, D. R., et al. (2013). *Ceres syn1deg-day terra-aqua modis edition 4a*. NASA Langley Atmospheric Science Data Center DAAC. doi: 10.5067/CERES/SYN1deg-Day\_Terra-Aqua\_Edition4A
- Emanuel, K., Wing, A. A., & Vincent, E. M. (2014, 2). Radiative-convective instability. *Journal of Advances in Modeling Earth Systems*, 6(1), 75-90. Retrieved from <http://dx.doi.org/10.1002/2013MS000270> doi: 10.1002/2013ms000270
- Eyring, V., Bony, S., Meehl, G. A., Senior, C. A., Stevens, B., Stouffer, R. J., & Taylor, K. E. (2016). Overview of the coupled model intercomparison project phase 6 (cmip6) experimental design and organization. *Geoscientific Model Development*, 9(5), 1937-1958. Retrieved from <https://gmd.copernicus.org/articles/9/1937/2016/> doi: 10.5194/gmd-9-1937-2016
- Hartmann, D. L., Hendon, H. H., & Houze, R. A. (1984). Some implications of the mesoscale circulations in tropical cloud clusters for large-scale dynam-

- 777       ics and climate.     *Journal of Atmospheric Sciences*, 41, 113 - 121.     Retrieved  
 778       from [https://journals.ametsoc.org/view/journals/atsc/41/1/1520-0469\\_1984\\_041\\_0113\\_siotsmc\\_2.0.co\\_2.xml](https://journals.ametsoc.org/view/journals/atsc/41/1/1520-0469_1984_041_0113_siotsmc_2.0.co_2.xml)     doi: 10.1175/1520-0469(1984)041(0113:  
 780       SIOTMC)2.0.CO;2
- 781       Hausfather, Z., Marvel, K., Schmidt, G. A., Nielsen-Gammon, J. W., & Zelinka, M.  
 782       (2022). Climate simulations: Recognize the ‘hot model’ problem.     *Nature*, 605,  
 783       26–29. doi: 10.1038/d41586-022-01192-2
- 784       Hersbach, H., Bell, B., Berrisford, P., Horányi, A., Muñoz-Sabater, J., Nicolas, J., ...  
 785       Thépaut, J.-N. (2023). *Era5 hourly data on pressure levels from 1940 to present*.  
 786       Copernicus Climate Change Service (C3S) Climate Data Store.     Retrieved from  
 787       <https://cds.climate.copernicus.eu/datasets/reanalysis-era5-pressure-levels> (Accessed: 2025-05-07) doi: 10.24381/cds.bd0915c6
- 789       Holloway, C. E., Wing, A. A., Bony, S., Muller, C., Masunaga, H., L'Ecuyer, T. S.,  
 790       ... Zuidema, P. (2017, November). Observing convective aggregation.     *Surveys  
 791       in Geophysics*, 38(6), 1199–1236.     Retrieved from <https://link.springer.com/article/10.1007/s10712-017-9419-1> doi: 10.1007/s10712-017-9419-1
- 793       Huang, B., Yin, X., Menne, M. J., Vose, R. S., & Zhang, H.-M. (2024). *Noaa global  
 794       surface temperature dataset (noaaglobaltemp), version 6.0*.     NOAA National Cen-  
 795       ters for Environmental Information.     Retrieved from <https://www.ncei.noaa.gov/access/metadata/landing-page/bin/iso?id=gov.noaa.ncdc%3AC01704>  
 796       doi: 10.25921/rzxg-p717
- 797       Huffman, G. J., Adler, R. F., Behrangi, A., Bolvin, D. T., Nelkin, E. J., Gu, G.,  
 798       & Ehsani, M. R. (2023). *The new version 3.2 global precipitation climatol-  
 799       ogy project (gpcp) monthly and daily precipitation products* (Vol. 36) (No. 21).  
 800       American Meteorological Society.     Retrieved from <https://doi.org/10.1175/JCLI-D-23-0123.1> doi: 10.1175/JCLI-D-23-0123.1
- 803       Jones, P. W. (1999). First- and second-order conservative remapping schemes  
 804       for grids in spherical coordinates.     *Monthly Weather Review*, 127(9), 2204  
 805       - 2210.     Retrieved from [https://journals.ametsoc.org/view/journals/mwre/127/9/1520-0493\\_1999\\_127\\_2204\\_fasocr\\_2.0.co\\_2.xml](https://journals.ametsoc.org/view/journals/mwre/127/9/1520-0493_1999_127_2204_fasocr_2.0.co_2.xml) doi: 10.1175/  
 806       1520-0493(1999)127(2204:FASOCR)2.0.CO;2
- 807       Koldunov, N., Kölling, T., Pedruzo-Bagazgoitia, X., Rackow, T., Redler, R.,  
 808       Sidorenko, D., ... Ziemen, F. A. (2023). *nextgems: output of the model de-  
 809       velopment cycle 3 simulations for icon and ifs*.     World Data Center for Cli-  
 810       mate (WDCC) at DKRZ.     Retrieved from [https://doi.org/10.26050/WDCC/nextGEMS\\_cyc3](https://doi.org/10.26050/WDCC/nextGEMS_cyc3) doi: 10.26050/WDCC/nextGEMS\_cyc3
- 813       Maddox, R. A. (1980, November). Meoscale convective complexes.     *Bulletin of  
 814       the American Meteorological Society*, 61(11), 1374–1387.     Retrieved from [http://dx.doi.org/10.1175/1520-0477\(1980\)061<1374:MCC>2.0.CO;2](http://dx.doi.org/10.1175/1520-0477(1980)061<1374:MCC>2.0.CO;2) doi: 10.1175/  
 815       1520-0477(1980)061<1374:mcc>2.0.co;2
- 817       Mapes, B. E. (1993, July). Gregarious tropical convection.     *Journal of the At-  
 818       mospheric Sciences*, 50(13), 2026–2037.     Retrieved from [http://dx.doi.org/10.1175/1520-0469\(1993\)050<2026:GTC>2.0.CO;2](http://dx.doi.org/10.1175/1520-0469(1993)050<2026:GTC>2.0.CO;2) doi: 10.1175/1520-0469(1993)  
 819       050<2026:gtc>2.0.co;2
- 821       Mapes, B. E., & Houze, R. A. (1993, May). Cloud clusters and superclusters  
 822       over the oceanic warm pool.     *Monthly Weather Review*, 121(5), 1398–1416.  
 823       Retrieved from [http://dx.doi.org/10.1175/1520-0493\(1993\)121<1398:ccasot>2.0.co;2](http://dx.doi.org/10.1175/1520-0493(1993)121<1398:CCASOT>2.0.CO;2) doi: 10.1175/1520-0493(1993)121<1398:ccasot>2.0.co;2
- 825       Mardia, K. V., Kent, J. T., & Bibby, J. M. (1979). *Multivariate analysis*. London:  
 826       Academic Press.
- 827       Pendergrass, A. G., Reed, K. A., & Medeiros, B. (2016). The link between extreme  
 828       precipitation and convective organization in a warming climate: Global radiative-  
 829       convective equilibrium simulations.     *Geophysical Research Letters*, 43(21), 11,445-  
 830       11,452.     Retrieved from <https://agupubs.onlinelibrary.wiley.com/doi/abs/>

- 831            10.1002/2016GL071285 doi: <https://doi.org/10.1002/2016GL071285>
- 832       Popp, M., & Bony, S. (2019). Stronger zonal convective clustering associated with a  
833       wider tropical rain belt. *Nature Communications*, 10, 4261. doi: 10.1038/s41467  
834       -019-12167-9
- 835       Quan, H., Zhang, B., Wang, C., & Fueglistaler, S. (2025). The sea surface tem-  
836       perature pattern effect on outgoing longwave radiation: The role of large-scale  
837       convective aggregation. *Geophysical Research Letters*, 52(11), e2024GL112756.  
838       Retrieved from <https://agupubs.onlinelibrary.wiley.com/doi/abs/10.1029/2024GL112756> (e2024GL112756) doi: <https://doi.org/10.1029/2024GL112756>
- 841       Retsch, M. H., Jakob, C., & Singh, M. S. (2020, 4). Assessing convective organiza-  
842       tion in tropical radar observations. *Journal of Geophysical Research: Atmospheres*,  
843       125. doi: 10.1029/2019JD031801
- 844       Ropelewski, C., & Jones, P. (1987). An extension of the tahiti–darwin southern os-  
845       cillation index. *Monthly Weather Review*, 115, 2161–2165.
- 846       Schiro, K., Su, H., Ahmed, F., Dai, N., Singer, C., Gentine, P., ... Neelin, J.  
847       (2022, 11). Model spread in tropical low cloud feedback tied to overturning  
848       circulation response to warming. *Nature Communications*, 13, 7119. Retrieved  
849       from <https://www.nature.com/articles/s41467-022-34787-4> doi:  
850       10.1038/s41467-022-34787-4
- 851       Semie, A. G., & Bony, S. (2020). Relationship between precipitation extremes  
852       and convective organization inferred from satellite observations. *Geophysical  
853       Research Letters*, 47(9), e2019GL086927. Retrieved from <https://agupubs.onlinelibrary.wiley.com/doi/abs/10.1029/2019GL086927> (e2019GL086927)  
854       10.1029/2019GL086927 doi: <https://doi.org/10.1029/2019GL086927>
- 855       Sobel, A. H., Held, I. M., & Bretherton, C. S. (2002). The enso signal in tropical  
856       tropospheric temperature. *Journal of Climate*, 15(18), 2702 - 2706. Retrieved  
857       from [https://journals.ametsoc.org/view/journals/clim/15/18/1520-0442\\_2002\\_015\\_2702\\_tesitt\\_2.0.co\\_2.xml](https://journals.ametsoc.org/view/journals/clim/15/18/1520-0442_2002_015_2702_tesitt_2.0.co_2.xml) doi: 10.1175/1520-0442(2002)015<2702:TESITT>2.0.CO;2
- 861       Tobin, I., Bony, S., Holloway, C. E., Grandpeix, J.-Y., Sèze, G., Coppin, D., ...  
862       Roca, R. (2013). Does convective aggregation need to be represented in cumulus  
863       parameterizations? *Journal of Advances in Modeling Earth Systems*, 5(4), 692-  
864       703. Retrieved from <https://agupubs.onlinelibrary.wiley.com/doi/abs/10.1002/jame.20047> doi: <https://doi.org/10.1002/jame.20047>
- 866       Tselioudis, G., Tromeur, E., Rossow, W. B., & Zerefos, C. S. (2010, 7). Decadal  
867       changes in tropical convection suggest effects on stratospheric water vapor. *Geo-  
868       physical Research Letters*, 37. doi: 10.1029/2010GL044092
- 869       Watanabe, M., Kang, S. M., Collins, M., Hwang, Y.-T., McGregor, S., & Stuecker,  
870       M. F. (2024). Possible shift in controls of the tropical pacific surface warming  
871       pattern. *Nature*, 630(8016), 315–324. Retrieved from <https://www.nature.com/articles/s41586-024-07452-7> doi: 10.1038/s41586-024-07452-7
- 873       Wheeler, M., & Kiladis, G. N. (1999). Convectively coupled equatorial waves: Anal-  
874       ysis of clouds and temperature in the wavenumber-frequency domain. *Journal  
875       of the Atmospheric Sciences*, 56, 374-399. Retrieved from [https://journals.ametsoc.org/view/journals/atsc/56/3/1520-0469\\_1999\\_056\\_0374\\_ccewao\\_2.0.co\\_2.xml](https://journals.ametsoc.org/view/journals/atsc/56/3/1520-0469_1999_056_0374_ccewao_2.0.co_2.xml) doi: 10.1175/1520-0469(1999)056<0374:CCEWAO>2.0.CO;2
- 878       Williams, A. I. L., Jeevanjee, N., & Bloch-Johnson, J. (2023). Circus tents, con-  
879       vective thresholds, and the non-linear climate response to tropical sssts. *Geophys-  
880       ical Research Letters*, 50(6), e2022GL101499. Retrieved from <https://agupubs.onlinelibrary.wiley.com/doi/abs/10.1029/2022GL101499> (e2022GL101499)  
881       2022GL101499 doi: <https://doi.org/10.1029/2022GL101499>
- 883       Wills, R. C. J., Dong, Y., Proistosecu, C., Armour, K. C., & Battisti, D. S. (2022,  
884       September). Systematic climate model biases in the large-scale patterns of recent

- 885 sea-surface temperature and sea-level pressure change. *Geophysical Research Letters*, 49(17). Retrieved from <http://dx.doi.org/10.1029/2022GL100011> doi:  
886 10.1029/2022gl100011  
887 Wing, A. A., Emanuel, K., Holloway, C. E., & Muller, C. (2018). Convective  
888 self-aggregation in numerical simulations: A review. In R. Pincus, D. Winker,  
889 S. Bony, & B. Stevens (Eds.), *Shallow clouds, water vapor, circulation, and*  
890 *climate sensitivity* (pp. 1–25). Cham: Springer International Publishing.  
891 Retrieved from [https://doi.org/10.1007/978-3-319-77273-8\\_1](https://doi.org/10.1007/978-3-319-77273-8_1) doi:  
892 10.1007/978-3-319-77273-8\_1  
893 Wing, A. A., & Emanuel, K. A. (2014). Physical mechanisms controlling self-  
894 aggregation of convection in idealized numerical modeling simulations. *Journal*  
895 *of Advances in Modeling Earth Systems*, 6(1), 59–74. Retrieved from  
896 <https://agupubs.onlinelibrary.wiley.com/doi/abs/10.1002/2013MS000269>  
897 doi: <https://doi.org/10.1002/2013MS000269>  
898 Wodzicki, K. R., & Rapp, A. D. (2016). Long-term characterization of  
899 the pacific itcz using trmm, gpcp, and era-interim. *Journal of Geophysi-*  
900 *cal Research: Atmospheres*, 121(7), 3153–3170. Retrieved from <https://agupubs.onlinelibrary.wiley.com/doi/abs/10.1002/2015JD024458> doi:  
901 <https://doi.org/10.1002/2015JD024458>  
902 Young, A. H., Knapp, K. R., Inamdar, A., Hankins, W., & Rossow, W. B. (2018).  
903 The international satellite cloud climatology project h-series climate data record  
904 product. *Earth System Science Data*, 10(1), 583–593. Retrieved from <https://essd.copernicus.org/articles/10/583/2018/> doi: 10.5194/essd-10-583-2018  
905 Zelinka, M. D., Myers, T. A., McCoy, D. T., Po-Chedley, S., Caldwell, P. M., Cesspi,  
906 P., ... Taylor, K. E. (2020). Causes of higher climate sensitivity in cmip6 models.  
907 *Geophysical Research Letters*, 47(1), e2019GL085782. Retrieved from <https://agupubs.onlinelibrary.wiley.com/doi/full/10.1029/2019GL085782>  
908  
909  
910  
911